Mineralogical evolution of a weathering profile in the Tagaung Taung Ni laterite deposit: Significance of smectite in the formation of high-grade Ni ore in Myanmar

Ayaka Murofushi[1], Tsubasa Otake[1*], Kenzo Sanematsu[2], Kyaw Zay Ya[3], Akane Ito[4], Ryosuke Kikuchi[1], Tsutomu Sato[1]

[1]Division of Sustainable Resource Engineering, Faculty of Engineering, Hokkaido University, N13W8, Kita-ku, Sapporo, Hokkaido, 060-8628, Japan

[2]Institute for Geo-Resources and Environment, National Institute of Advanced Industrial Science and Technology (AIST), Central-7, Higashi 1-1-1, Tsukuba, Ibaraki 305-8567, Japan

[3]Department of Geological Survey and Mineral Exploration (DGSE), Ministry of Natural Resources and Environmental Conservation, Myanmar Gems Museum, Naypitaw, Myanmar

[4]Department of Applied Chemistry for Environment, School of Science and Technology, Kwansei Gakuin University, Gakuen 2-1, Sanda, Hyogo, 669-1337, Japan

*Corresponding author: Tsubasa Otake

Division of Sustainable Resources Engineering, Faculty of Engineering, Hokkaido University, N13W8, Kita-ku, Sapporo 060-8628, Japan

Phone: 011-706-6323; fax: 011-706-6323; e-mail: totake@eng.hokudai.ac.jp

ORCID: 0000-0001-9596-4141

Abstract

Myanmar has a drier sub-tropical climate than countries that typically contain Ni laterite deposits, but hosts a Ni laterite deposit at Tagaung Taung. Given that Ni enrichment processes in the Tagaung Taung deposit are poorly understood, we investigated the geochemical and mineralogical evolution of two weathering profiles developed on different bedrocks in the central part of Myanmar: a partly serpentinized harzburgite at Tagaung and an almost completely serpentinized peridotite at Budaung. The whole-rock geochemical data indicate that Si was retained relative to Fe and Al in the weathering profiles. Nickel has been enriched to contents as high as 4.89 wt.% NiO in the saprolite layers at Tagaung, whereas the saprolite layers at Budaung contain ≤1.55 wt.% NiO. Smectite is the main mineral that formed in the saprolite layers at Tagaung, whereas secondary serpentine dominates the saprolite layers at Budaung. Microscopic observations indicate that Ni-smectite (>10 wt.% NiO), which is only observed at Tagaung, formed as a replacement product of orthopyroxene. In addition to the high Ni fixation capacity of smectite relative to secondary serpentine, Ni-rich pore water derived from the dissolution of olivine likely contributed to the high Ni contents of smectite. Our results imply that high-grade Ni laterite deposits may develop on unaltered or partly serpentinized harzburgite under the climatic conditions typical of Myanmar.

Keywords: Chemical weathering; Harzburgite; Pyroxene; Nickel; Smectite; Laterite; Myanmar

Introduction

Nickel (Ni) laterite deposits form by intense chemical weathering of ultramafic rocks in a tropical or sub-tropical climate. Among different types of Ni laterite deposits, hydrous Mg silicate deposits are the most common, and they tend to produce the highest ore grades (2–5 wt.% Ni; Butt and Cluzel 2013). In general, during the chemical weathering of ultramafic rocks, Fe becomes concentrated towards the top of the weathering profile due to the loss of Si and Mg. As a result, Fe-(hydr)oxides are formed mainly in the laterite, strongly weathered upper horizon, whereas Mg–Ni silicate minerals characterize the saprolite, weakly weathered lower horizon (Butt and Cluzel 2013; Freyssinet et al. 2005; Golightly 1981; 2010).

The distribution of Ni in weathering profiles is influenced by many factors, such as bedrock lithology, tectonic setting, drainage, and climate (Butt and Cluzel 2013; Gaudin et al. 2005; Gleeson et al. 2003; Golightly 1981; 2010; Maurizot et al. 2019; Thorne et al. 2012). Most Ni laterite deposits develop under a humid tropical climate where intense chemical weathering leads to considerable mobilization of Ni into saprolite layers. In a typical hydrous Mg silicate deposit, serpentine is regarded as one of the main Ni-bearing minerals of the ore zone (Dublet et al. 2012; Freyssinet et al. 2005; Ito et al. 2021). However, Ni released from primary bedrock minerals is retained in Fe-(hydr)oxides during the initial stage of chemical weathering, and this Ni is redistributed from the Fe-(hydr)oxides into serpentine in the saprolite as chemical weathering progresses (Freyssinet et al. 2005; Villanova-de-Benavent et al. 2017). This process is critical for the formation of Ni ores in saprolite (Ito et al. 2021).

However, it is not clear whether this process is important under different climatic conditions, such as the drier sub-tropical climate of Myanmar, because the drier

conditions might produce different weathering products. Tagaung Taung, which was discovered in 1981, is the only Ni laterite deposit currently being mined in Myanmar. Schellmann (1989a, b) classified the Tagaung Taung deposit as a hydrous Mg silicate deposit, consisting primarily of a relatively thick saprolite layer containing serpentine and smectite. However, the mineralogical evolution during the formation of the ore deposit remains poorly understood**.**

Therefore, the objectives of our study were to understand the formation processes of weathering products in the Tagaung Taung deposit, and their role in Ni enrichment and high-grade ore formation. To achieve our objectives, we compared the geochemical and mineralogical characteristics of two contrasting weathering profiles developed on different bedrocks, specifically those at Tagaung Taung and Budaung. Although Budaung in the Kyaukpahto area is located on an almost completely serpentinized ultramafic complex close to Tagaung Taung, our preliminary investigation indicates that no high-grade Ni ore deposit has developed at this locality.

Study sites

The Tagaung Taung and Kyaukpahto areas are located in the Mandalay and Sagaing regions, respectively, and both are ~200 km north of Mandalay city in the central part of Myanmar (Fig. 1a). They are only ~50 km apart across the Ayeyarwady River (Fig. 1b). Annual precipitation and the average temperature around Tagaung Taung are ~1300 mm and ~30 °C, respectively (Schellmann 1989b).

Geological setting

Ophiolitic rocks occur in three sub-parallel belts that trend nearly N–S in Myanmar:

93 the Western Ophiolite Belt (WOB), Central Ophiolite Belt (COB), and Eastern Ophiolite
94 Belt (EOB; Fig.1a; Hla Htay et al. 2017). Hla Htay et al. (2017) suggested that the WOB
95 and COB represent a single ophiolite line, called the Myanmar Ophiolite Line (MOL),
96 which formed during the Cretaceous and Jurassic and separated during the middle
97 Miocene into the WOB and COB as a result of dextral movement on the Sagaing Fault.
98 The EOB is thought to have remained in its original position adjacent to the MOL.
99 The Tagaung Taung area is part of the EOB (Fig.1b; Hla Htay et al. 2017; Khin Zaw
100 et al. 2017; MGS 2014). The ore reserves of the Tagaung Taung deposit were estimated
101 to be 40 million tons at an average grade of 2 wt.% Ni (Schellmann 1989b). The main ore
102 zone contains saprolite with an average thickness of 7–8 m (up to 24 m thick) that is
103 overlain by laterite with an average thickness of 8 m (Schellmann 1989b; Soe Win et al.
104 2014). In contrast, the Kyaukpahto area, where Budaung is located, is part of the COB
105 (Hla Htay et al. 2017). Laterite is less developed in this area as compared with Tagaung
106 Taung. The studied weathering profiles in the Kyaukpahto and Tagaung Taung areas are
107 located at 23°46.26” N, 95°59.29” E and 23°34.404” N, 96°08.118” E, respectively.
108 Hereafter, the weathering profiles at Budaung and Tagaung Taung are referred to as
109 Budaung and Tagaung, respectively.
110
111 Weathering profiles
112 *Budaung*
113 The weathering profile at Budaung is ~8 m thick and consists of a thick saprolite
114 layer (~6 m) and a thinner laterite layer (~2 m; Fig. 2a). The bedrock is mainly a dark
115 greenish serpentinite, which is likely a metamorphosed harzburgite. The saprolite can be
116 subdivided into three layers, lower, middle, and upper. In the lower saprolite layer,

117 macroscopic structures in the bedrock are still visible with light green to white coloration,
118 while brown to orange colored rock fragments occur in the upper saprolite layer. Above
119 the saprolite layer, the laterite layer is characterized by brownish, fine, porous texture.
120
121 *Tagaung*
122 The weathering profile we studied is developed near the top of Tagaung Taung.
123 Because the bottom of the observed section was weathered, bedrock could not be sampled
124 at this section. Instead, we collected an unweathered sample of bedrock in the foothills of
125 Tagaung Taung. The thickness of the observed weathering profile is ~12 m, with a
126 relatively thick saprolite layer (~9 m) and a thinner laterite layer (~3 m; Fig. 2b). The
127 bedrock is a massive, partly serpentinized harzburgite that is dark blue to black. The
128 saprolite layer consists mainly of brownish fine grains, and it often appears like a wet
129 mud, indicating the presence of expansive clays. No primary bedrock textures were
130 observed even in the lower saprolite layer.
131
132 **Samples and analytical methods**
133 Samples
134 Samples of bedrock and weathered material were collected for chemical and
135 mineralogical analyses at 1–3 m intervals in the depth profiles, and six and nine samples
136 were collected at Budaung and Tagaung, respectively (Fig. 2). Samples were taken from
137 the bedrock, the lower, middle and upper saprolite layers, and the laterite layer.
138
139 Analytical methods
140 Bedrock samples were crushed to less than ~2 mm with a hammer and washed with

141 acetone and distilled water. All the samples, including the crushed bedrock, saprolite and
142 laterite samples, were dried at 40 °C, then pulverized to less than ~75 μm using agate rods
143 in polycarbonate tubes with Multi-Beads Shocker equipment (PV1001(s), Yasui Kikai).
144 To determine the amount of structurally bonded water in the bedrock samples, the mass
145 change was measured on ~1 g of the pulverized samples by heating at 850 °C for 10 h in
146 a muffle furnace after preheating at 110 °C for 2 h.
147 To determine the whole-rock mineralogy, X-ray diffraction (XRD; Multi Flex,
148 Rigaku) with graphite-monochromatic incident Cu-Kα radiation at 40 kV and 30 mA was
149 used on ~3 g of each pulverized sample. The XRD patterns were scanned from 5° to 70°
150 (2θ) with a scanning speed of 2.0°/min. To identify the clay minerals, fine (<2 μm)
151 fractions of the unpulverized saprolite samples were obtained using ultrasonic dispersion
152 and centrifugation. These <2 μm fractions dispersed in deionized water were dropped
153 onto a glass plate and dried at room temperature to create samples with a preferred mineral
154 orientation. The XRD patterns of these oriented samples before and after ethylene glycol
155 (EG) treatment were obtained by XRD (RINT 2000, Rigaku) with Cu-Kα radiation at 30
156 kV and 20 mA, following the methods of Shimbashi et al. (2018).
157 Loss-on-ignition (LOI) values were determined from the weight loss of powdered
158 samples after heating at 1100 °C for 10 h. These dried samples were then used for whole-
159 rock geochemical analysis. X-ray fluorescence (XRF) analyses were conducted on fused
160 glass beads with a Rigaku ZSX Primus III+ at AIST and Spectoris MagiX PRO at
161 Hokkaido University for the Budaung and Tagaung samples, respectively. The analytical
162 conditions were described in previous studies (Chikanda et al. 2019; Tupaz et al. 2020).
163 To estimate the losses and gains of Si, Mg, Fe, Al, and Ni relative to the bedrocks, mass
164 transfer coefficients ($\tau_{j,w}$) were calculated based on the following equation:

$$\tau_{j,w} = \frac{C_{j,w} \times C_{i,p}}{C_{j,p} \times C_{i,w}} - 1 \quad (1),$$

where C is the concentration (wt.%) of element *j* or *i*. The subscripts *j*, *i*, *p*, and *w* indicate mobile elements, immobile elements, bedrock samples, and weathered samples, respectively (Brimhall and Dietrich 1987). We selected Ti as the immobile element.

Mineral phases and textural features were observed in polished thin sections of representative samples under an optical microscope (Olympus BX60) and a scanning electron microscope coupled to an energy dispersive spectrometer (SEM–EDS; JSM-6510LA, JEOL). Field emission electron probe microanalyses (FE–EPMA; JXA-8530F, JEOL) were undertaken to quantify the chemical compositions of silicate minerals in the thin sections. Silicate mineral phases, including primary minerals and weathering products, were identified based on the measured (Mg + Fe + Ni)/Si ratios as compared with the stoichiometric ratios. The occupancy of octahedral and tetrahedral sites for these minerals was taken from Deer et al. (1982, 2009), Morimoto (1988), and Wilson et al. (2013). Iron in the weathering products, such as secondary serpentine and smectite, was assumed to be Fe^{3+} (Decarreau et al. 1987; Gaudin et al. 2005; Roqué-Rosell et al. 2017). The amounts of Fe^{2+} determined by $KMnO_4$ titration (Goldich 1984) were minor in representative bulk weathered samples (14% and 3% of the total Fe in a serpentine-dominated sample [2607] and a smectite-dominated sample [2910], respectively), which suggests this assumption is reasonable. Given that the studied smectite is deficient in Ca, Na, and K, we used Mg as the dominant interlayer cation to make the interlayer charge 0.33 (i.e., the ideal smectite composition).

Some of the weathering products yielded poor element totals from the EPMA analyses, probably due to their porous structure and/or high water content; consequently, their chemical compositions were obtained semi-quantitatively by SEM–EDS without

189 standard calibration. Such products typically have a range of (Mg + Fe + Ni)/Si ratios
190 (0.9–1.3) that did not correspond to the stoichiometric ratios of the aforementioned
191 minerals. As such, we use terms such as Fe–Al silicates or Mg–Fe–Ni silicates, based on
192 the chemical compositions, rather than identifying specific mineral phases.
193
194 **Results**
195 Characterization of bedrock
196 The amount of structurally bonded water in the bedrock at Budaung (12.0 wt.%)
197 was higher than that at Tagaung (7.9 wt.%), corresponding to ~92% and 60% on the
198 degree of serpentinization at Budaung and Tagaung, respectively (Kyser et al. 1999;
199 Pereira et al. 2008). Observations under the petrographic microscope confirmed the
200 presence of serpentine with minor amounts of fine-grained chromite and magnetite in the
201 bedrocks (Fig. 3a, b). Olivine and orthopyroxene were also commonly observed in the
202 Tagaung bedrock. The olivine grains were partly altered to serpentine and exhibit a mesh
203 structure (Fig. 3b), whereas the orthopyroxene was relatively unaltered (Fig. 3c).
204
205 Whole-rock mineralogy
206 *Budaung*
207 The powder XRD analyses show that serpentine is dominant in the saprolite layer,
208 but decreases gradually in abundance towards the top of the profile (Fig. 4a). In addition,
209 a small 15 Å clay mineral peak, corresponding to 5.9° 2θ CuKα, was detected in all the
210 saprolite samples. The XRD results of oriented samples of the <2 μm fraction yielded a
211 clearer peak for this 15 Å clay mineral (Fig. 4b). Given that the peak at ~15.2 Å shifted
212 to ~17.3 Å with EG treatment, the 15 Å clay mineral is identified as smectite. At the

213 bottom of the laterite layer, both quartz and serpentine were identified in the XRD profile,
214 but in the top-most sample, only peaks for quartz were observed (Fig. 4a).
215
216 *Tagaung*
217 The XRD results show that peaks for olivine are absent in the lower saprolite layer,
218 whereas peaks for serpentine and orthopyroxene are present throughout the saprolite,
219 even in the upper saprolite layer (Fig. 4c). Smectite was dominant in all saprolite samples.
220 The 060 reflections show broad peaks ~1.51 Å (Fig. 4d), indicating that it is an Fe-rich
221 dioctahedral smectite. Although quartz occurs as a minor mineral in the saprolite samples,
222 its peak intensities increased significantly in the laterite layer. In the laterite layer, peaks
223 for quartz, goethite, and hematite dominate over minor peaks for a micaceous mineral.
224
225 Whole-rock geochemistry
226 *Budaung*
227 Whereas the bedrock at Budaung contains ~40 wt.% SiO_2 and ~40 wt.% MgO, the
228 MgO content drops significantly from the saprolite (~31 wt.%) to the laterite layers (~2.6
229 wt.%; Fig. 5a; Supplementary Table 1). In contrast, SiO_2 contents increase from the
230 saprolite (~41 wt.%) to the laterite layers (~64 wt.%). The Fe_2O_3 and Al_2O_3 contents
231 increase gradually towards the top of the profile (up to ~19 wt.% and ~7 wt.%,
232 respectively). The NiO content increases to 1.55 wt.% in the saprolite layer (average ~1.4
233 wt.%), then decreases in the laterite layer (~0.7 wt.%).
234 The mass transfer coefficients ($\tau_{j,Ti}$ values) for all the major elements Si, Mg, Fe,
235 and Al are negative throughout the profile (Fig. 5a), indicating that these elements were
236 lost from the profile. The $\tau_{j,Ti}$ values for Ni are also negative for all the samples except

for one in the lower saprolite, indicating that gains in Ni were minimal in the profile.

Tagaung

The MgO contents in the saprolite and laterite layers at Tagaung are much lower (~11 and ~1.7 wt.%, respectively; Fig. 5b; Supplementary Table 1) than those at Budaung. The SiO_2 contents decrease slightly from the saprolite (~37 wt.%) to the laterite layers (~29 wt.%). The Fe_2O_3 and Al_2O_3 behave similarly to Budaung, but the saprolite and laterite layers have much higher Fe_2O_3 contents (~25 and ~45 wt.%, respectively). The NiO content is as high as 4.89 wt.% in the saprolite layer. The average contents of NiO in the saprolite and laterite layers are ~4.5 and ~1.7 wt.%, respectively.

The $\tau_{j,Ti}$ values for Si and Mg are all negative, particularly in the laterite layer (Fig. 5b). The $\tau_{j,Ti}$ values for Fe and Al are positive at some points in the saprolite layer, but negative (close to −1) in the laterite layer. The $\tau_{j,Ti}$ values for Ni in the saprolite layer are high (up to 15.3), indicating a significant gain of Ni in the saprolite layer, but then drop to almost −1 in the laterite layer.

Chemical composition of silicate minerals

Budaung

The EPMA analysis show that the NiO content of serpentine in the bedrock is low, ~0.05 wt.% (Supplementary Table 2). Two types of serpentine were recognized in the lower and upper saprolite layers: Fe- and Ni-poor primary serpentine (Ser-I) and Fe- and Ni-rich secondary serpentine (Ser-II). The NiO contents of Ser-II are similar in the lower and upper saprolite layers, varying from 1.59 to 2.21 wt.% and 1.66 to 2.19 wt.%, respectively (Fig. 6a). Ser-II in both the lower and upper saprolite layers contains more

Mg and less Fe and Ni than the smectite (Fig. 6b).

In contrast, the NiO contents of smectite in the upper saprolite layer tend to be much higher (1.69–2.59 wt.%) than those of smectite in the lower saprolite layer (1.50–2.17 wt.%) or Ser-II in the upper saprolite layer (Fig. 6a). Smectite in both the lower and upper saprolite layers is more Fe-rich than the Ser-II (Fig. 6b). The average structural formulae of smectite are $Mg_{0.16}(Si_{3.47}, Al_{0.11}, Fe^{3+}_{0.42})(Fe^{3+}_{0.80}, Mg_{1.75}, Ni_{0.12})O_{10}(OH)_2$ and $(Mg_{0.16}, K_{0.01})(Si_{3.72}, Fe^{3+}_{0.28})(Fe^{3+}_{0.88}, Mg_{1.46}, Ni_{0.14})O_{10}(OH)_2$, respectively (Supplementary Table 2). Given that smectite contains abundant Mg and Fe^{3+} in their octahedral sheets, it is identified as Fe–Mg smectite. The number of cations in the octahedral sites (ΣOct.) of smectite varies from 2.22 to 2.93, which falls within the range for trioctahedral smectite or is intermediate between dioctahedral and trioctahedral smectite (Fig. S1; Meunier 2005).

In the laterite layer, Fe–Al silicates were observed with variable chemical compositions (Fig. S2). Ni was not detected in the Fe–Al silicate phases.

Tagaung

In Tagaung bedrock, olivine, orthopyroxene, and Ser-I contain ~0.39, ~0.10, and ~0.21 wt.% NiO, respectively (Supplementary Table 3). Olivine is the primary mineral with the highest concentrations of Ni. The NiO contents of the smectite are quite variable, ranging from 1.16 to 33.9 wt.% (Fig. 6c, d). We classified the smectite with >10 wt.% NiO as Ni-smectite.

Ni-smectite was observed in both the lower and upper saprolite layers. Ni-smectite in the upper saprolite layer tend to have higher NiO contents (20.1–33.9 wt.%) than those in the lower saprolite layer (14.9–18.1 wt.%). The NiO content increases with decreasing

Fe_2O_3 content (Fig. 6c). The average structural formulae of Ni-smectite in the lower and upper saprolite layers are $Mg_{0.16}Si_{4.02}(Al_{0.01}, Fe^{3+}_{0.83}, Mg_{0.48}, Ni_{1.03})O_{10}(OH)_2$ and $(Mg_{0.16}, Ca_{0.01})(Si_{3.76}, Al_{0.03}, Fe^{3+}_{0.20})(Fe^{3+}_{0.43}, Mg_{0.48}, Ni_{1.8})O_{10}(OH)_2$, respectively (Supplementary Table 3). The ΣOct. values of Ni-smectite in the lower and upper saprolite layers range from 2.27 to 2.40 and 2.61 to 2.95, respectively, mostly falling within the range for trioctahedral smectite (Fig. S1).

A Fe-smectite with low Ni content was also observed as a weathering product of olivine and orthopyroxene. In the lower saprolite layer, the NiO contents of Fe-smectite after olivine are 1.2–2.1 wt.%, whereas Fe-smectite after orthopyroxene has higher NiO contents (3.4–7.9 wt.%; Fig. 6d). There is no significant difference in the Fe_2O_3 contents of Fe-smectite. The average structural formulae of Fe-smectite after olivine and pyroxene in the lower saprolite layer are $(Mg_{0.14}, Ca_{0.02}, K_{0.03})(Si_{3.96}, Al_{0.02}, Fe^{3+}_{0.03})(Al_{0.01}, Fe^{3+}_{1.25}, Mg_{0.81}, Ni_{0.11})O_{10}(OH)_2$ and $(Mg_{0.14}, Ca_{0.02}, K_{0.02})(Si_{3.99}, Al_{0.01})(Al_{0.04}, Fe^{3+}_{1.20}, Mg_{0.66}, Ni_{0.29})O_{10}(OH)_2$, respectively (Supplementary Table 3). The NiO content of Fe-smectite in the upper saprolite layer is similar (5.28–9.95 wt.%), regardless of their occurrence (Fig. 6d). The average structural formulae of Fe-smectite after olivine and pyroxene in the upper saprolite layer are $(Mg_{0.14}, Ca_{0.01}, K_{0.03})(Si_{4.00}, Al_{0.01}, Fe^{3+}_{0.01})(Al_{0.01}, Fe^{3+}_{1.27}, Mg_{0.40}, Ni_{0.47})O_{10}(OH)_2$ and $(Mg_{0.15}, K_{0.01}, Ca_{0.01})(Si_{3.93}, Al_{0.04}, Fe^{3+}_{0.03})(Al_{0.03}, Fe^{3+}_{1.28}, Mg_{0.41}, Ni_{0.45})O_{10}(OH)_2$, respectively (Supplementary Table 3). The ΣOct. values of Fe-smectite range from 2.07 to 2.39 and 2.06 to 2.33 in the lower and upper saprolite layers, respectively (Supplementary Table 3), mostly falling within the range for dioctahedral smectite (Fig. S1).

Mg–Fe–Ni silicates were also observed in the saprolite layer. Their chemical compositions are variable, including their Fe_2O_3 and NiO contents (Fig. 6d). The Mg–

Fe–Ni silicates in the upper saprolite layer tend to contain more MgO and less Fe_2O_3 and NiO, when compared with those in the lower saprolite layer.

In the laterite layer, the chemical composition of the Fe–Al silicates is more variable that that at Budaung (Fig. S2). Nickel was only detected in samples with high Fe_2O_3 contents (e.g., >50 wt.%; Fig. S2d).

Silicate minerals in the saprolite and laterite layers

Budaung

SEM observations show that Ser-I occurs as relatively large (10–20 μm) individual crystals, whereas Ser-II appears to be much finer grained and in aggregates (Fig. 7a). The smectite is surrounded by Ser-II (Fig. 7b). In the upper saprolite layer, Ser-II was most commonly observed, followed by smectite and Ser-I. The Ser-II forms vein-like structures, and it appears to be more crystalline (Fig. 7c) than Ser-II in the lower saprolite (Fig. 7a), which commonly surrounds smectite (Fig. 7d) and Ser-I. In the laterite layer, Fe–Al silicates form aggregates while the quartz forms either 5–30 μm grains or ~100 μm wide veins (Fig. 7e).

Tagaung

In the lower saprolite layer, Ni-smectite occurs only at the rims of weathered orthopyroxene (Fig. 7f, g). In contrast, Fe-smectite coexists with a variety of primary and secondary minerals. Some Fe-smectite formed at the rims of weathered orthopyroxene, together with Ni-smectite (Fig. 7g), indicating that both formed after orthopyroxene. Fe-smectite was also observed in relics of olivine, and these therefore formed from olivine (Fig. 7h). Both the olivine and Fe-smectite appear to be surrounded by Mg–Fe–Ni

333 silicates.

334 In the upper saprolite layer, Ni-smectite was also observed near the remnants of
335 weathered orthopyroxene (Fig. 7i), developed in particulate form (Fig. 7j). Some of the
336 Fe-smectite occurs as porous materials in massive particulate form together with Ni-
337 smectite (Fig. 7i), whereas some appears to be surrounded by Mg–Fe–Ni silicates (Fig.
338 7k). These observations in both the lower and upper saprolite layers suggest that the Mg–
339 Fe–Ni silicates and coexisting Fe-smectite were derived from olivine, whereas the Ni-
340 smectite and coexisting Fe-smectite were derived from orthopyroxene. In the laterite layer,
341 Fe–Al silicates and quartz are similar to those at Budaung (Fig. 7l).

342

343 **Discussion**

344 Geochemical trends in the weathering profiles at Budaung and Tagaung

345 The whole-rock geochemical analyses of samples from the weathering profiles at
346 Budaung and Tagaung indicate that the laterite layers have high SiO_2 contents (Fig. 5a, b;
347 Supplementary Table 1). The molar Si–(Fe + Al)–Mg ternary diagram reveals a
348 geochemical evolution toward a Si-rich end-member as chemical weathering progresses
349 (Fig. 8a), which is different from the weathering profiles of Ni laterite deposits in other
350 areas such as Cuba, Dominican Republic, Indonesia, and Philippines (Aiglsperger et al.
351 2016; Delina et al. 2020; Golightly 1981; Ito et al. 2021). Given that the mass transfer
352 coefficients (τ values) indicate that Si was lost in the saprolite and laterite layers at
353 Budaung and Tagaung (Fig. 5), the high SiO_2 contents in the Myanmar profiles appear to
354 reflect differences in the degree of Si retention relative to Fe and Al.

355 The retention of Si was probably due primarily to the climatic conditions of
356 Myanmar, which has a longer dry season than Indonesia or the Philippines. This is

because more dissolved silica can be retained in the pore water of the weathering profile during a dry season. The relative enrichment of Si dictates the mineralogy of the weathering products in the laterite layers, which explains why Fe–Al silicates were commonly identified by SEM in the laterite layers at Budaung and Tagaung (Fig. 7e, l). A micaceous mineral, which is not a typical weathering product of ultramafic rocks, occurs in the laterite layer at Tagaung (Fig. 4c). This implies that part of the laterite layer was produced by physical weathering and transport, which also partly reflects the climatic conditions in Myanmar. The overlying sediments might also have contributed to the silica enrichment in the weathering profiles, since more Si-bearing pore water would have percolated down into the profiles. However, this effect is likely minor since retention of Si in the laterite layer was also documented in Budaung, where no micaceous mineral was identified (Fig. 4a).

A comparison of the two weathering profiles shows that the MgO contents of the saprolite layer at Budaung are higher than at Tagaung (Fig. 5), which suggests that chemical weathering was more intensive at Tagaung. This was probably due to differences in the mineralogical composition of their bedrocks. Almost completely serpentinized ultramafic rock, such as the bedrock at Budaung, is more resistant to chemical weathering because of the slower dissolution rate of serpentine relative to olivine and pyroxenes (Elias 2002; Golightly 1981; 2010).

The NiO contents of the saprolite layers are much higher (up to 4.89 wt.%) at Tagaung than those (up to 1.55 wt.%) at Budaung (Fig. 5). This may also partly reflect the fact that the weathering intensity is higher at Tagaung than Budaung. The mass transfer coefficients for Fe_2O_3 and NiO indicate that more Fe and Ni were gained in the saprolite layer at Tagaung than at Budaung (Fig. 5). The gains (or losses) for the whole

saprolite layer can be calculated using the following equation (Brimhall and Dietrich 1987):

$$m_j\ (kg) = \Sigma C_{j,p}\ \rho_p\ \tau_{j,w} D \quad (2),$$

where $C_{j,p}$ is the content of mobile element j in the bedrock sample, ρ_p is the bedrock density (2.6 ton/m^3 is used, after Schellmann 1989b), $\tau_{j,w}$ is the mass transfer coefficient of mobile element j (Eq. 1), and D is the thickness of the weathering profile (m). The Tagaung weathering profile shows a much larger gain in Ni relative to Fe (Ni/Fe = 290 kg/387 kg = ~0.75) compared with ratios of 0.05–0.22 in Indonesia (Fig. 8b; Ito et al. 2021).

The NiO contents of most Fe–Al silicates were below the detection limit of the SEM-EDS analyses (Fig. S2d), indicating the Fe–Al silicates contain little Ni. Only Fe–Al silicates with high Fe_2O_3 contents, which likely contain Fe-(hydr)oxides, contain a few wt.% NiO. Although previous studies have shown that Ni is concentrated in goethite within Ni laterite deposits by incorporation into the crystal structure and/or adsorption on its surface (Dublet et al. 2012; Fan and Gerson 2015), goethite is scarce in the laterite layer at Tagaung (Fig. 4c). Therefore, laterite layers in Myanmar likely have limited ability for Ni fixation. This is also supported by the mass transfer coefficients for Ni in the laterite layers, which are negative at both Tagaung and Budaung (Fig. 5).

Formation processes of the weathering products at Budaung and Tagaung

Ser-II was identified as the major weathering product that hosts Ni in the saprolite layers at Budaung, whereas Fe-smectite, Ni-smectite, and Mg–Fe–Ni silicates were the hosts of Ni in the saprolite layers at Tagaung. The preferential gain of Ni over Fe at Tagaung (Fig. 8b) suggests that smectite in the saprolite layer at Tagaung has a high Ni

405 fixation capacity.

406

407 Smectite

408 Although Fe-smectite is associated with both olivine and orthopyroxene, Ni-
409 smectite is only associated with orthopyroxene at Tagaung (Fig. 7f, h, i). Therefore, we
410 suggest that Fe-smectite formed from both olivine and orthopyroxene, whereas Ni-
411 smectite formed only from orthopyroxene. Olivine was almost completely weathered and
412 transformed into Fe-smectite in the lower saprolite layer at Tagaung (Figs 4c and 7h).
413 Although the morphology of the Fe-smectite does not appear to be different between the
414 lower and upper saprolite layers (Fig. 7h, k), NiO contents of the Fe-smectite tend to
415 increase from the lower (~1.7 ± 0.6 wt.%) to upper (~6.0 ± 1.0 wt.%) saprolite layer (Fig.
416 6d; Supplementary Table 3). The relationships among Fe, Mg, and Ni in the calculated
417 stoichiometry of the smectite indicate that occupancy of Mg in the octahedral sheet
418 decreases from the lower to upper saprolite layers, whereas no significant difference in
419 Fe occupancy was observed (Fig. 9a). Therefore, the Fe-smectite that was derived from
420 olivine in the lower saprolite layer was enriched in Ni by the progressive replacement of
421 Mg towards the upper saprolite layer.

422 In contrast, orthopyroxene is present in both the lower and upper saprolite layers at
423 Tagaung (Figs 4c and 7f, i). The coexisting Fe- and Ni-smectite in the lower saprolite
424 layer forms massive clusters of particulates that mimic the shape and size of
425 orthopyroxene crystals (Figs 3c and 7g), suggesting that both formed after orthopyroxene.
426 In contrast to the Fe-smectite that replaced olivine, some of the Fe-smectite that replaced
427 orthopyroxene is porous and therefore prone to further chemical weathering, although
428 some still occurs as massive particulates in the upper saprolite layer (Fig. 7i, j). These

429 different types of occurrence may have been caused by the slow weathering rate of the
430 pyroxene, which allowed different generations of Fe-smectite to be formed. The porous
431 Fe-smectite likely formed early in the lower saprolite layers, whereas the massive
432 particulate Fe-smectite formed at a later stage in the middle or upper saprolite layers. The
433 calculated stoichiometries of the Fe- and Ni-smectites indicate that the occupancy of Mg
434 in the octahedral sheet is largely consistent between the Ni- and Fe-smectite, whereas the
435 occupancy of Fe in the Ni-smectite was lower than in the Fe-smectite, particularly in the
436 upper saprolite layer (Fig. 9b).

437 Previous studies have also suggested that smectite commonly forms after pyroxene
438 during the chemical weathering of ultramafic rocks (Colin et al. 1990; Eggleton 1975).
439 Incongruent dissolution of pyroxene may cause the preferential formation of smectite as
440 a result of crystallographic similarities in the tetrahedral and octahedral structures
441 compared with other common Ni-bearing clay minerals (e.g., kerolite, sepiolite), and such
442 smectite can be abundant in weakly fractured zones under low water/rock ratio (Colin et
443 al. 1990). Silica-rich pore water may promote the incongruent dissolution of pyroxene,
444 leaving silica-chains in the solid phase as a precursor for the smectite. In addition, Fe
445 oxidation, which can occur in the pyroxene or be transported from the upper layers, likely
446 contributes to the formation of smectite, because smectite can contain more trivalent
447 cations than the other clay minerals.

448 The chemical compositions of smectite may have been strongly controlled by the
449 pore water chemistry during smectite formation. Fe–Mg smectite at Budaung may also
450 have formed from pyroxene, which is a minor constituent in the serpentinized harzburgite
451 bedrock at Budaung. The pore water at Budaung would not have been enriched in Ni
452 during the weathering of pyroxene, because the chemical weathering rate of pyroxene is

453 greater than that of serpentine. On the other hand, at Tagaung, olivine was weathered first,
454 followed by pyroxene and Ser-I. Given that olivine commonly contains more Ni than
455 pyroxene, the pore water at Tagaung during the transformation of pyroxene to smectite
456 would have been more Ni-rich than at Budaung. Because pyroxene would have been
457 transformed more slowly over a longer period of time in both the lower and upper
458 saprolite layers, the chemical composition of the pore water during the weathering of the
459 pyroxene would have been variable over time. In addition, Ni-smectite in the upper
460 saprolite layer appears to be more enriched in Ni than that in the lower saprolite layer
461 (Fig. 9b). Therefore, smectite that formed in the upper saprolite layer, during the late stage
462 of weathering, could be the most Ni-enriched smectite at Tagaung.
463
464 Serpentine-II
465 Two types of serpentine (i.e., Ser-I and -II) form as major minerals in the saprolite
466 at Budaung (Fig. 7a–d). Because the bedrock at Budaung contains only Ser-I, the Ser-I is
467 probably metamorphic in origin, and formed by serpentinization of harzburgite during
468 obduction of the COB ophiolite. On the other hand, the Ser-II, which is found only in the
469 saprolite, is almost certainly a weathering product. This is also supported by the
470 observation that Ser-I forms larger crystals than the finer grained Ser-II (Fig. 7a). The
471 EPMA results showed that Ser-II contains lower Mg and higher Ni (and Fe) contents than
472 Ser-I (Fig. 6b; Supplementary Table 2). Thus, Ser-I may have been transformed to Ser-II
473 by replacement of Mg by Ni (and Fe) in the octahedral sheet during chemical weathering
474 (Dublet et al. 2012; Fan and Gerson 2015; Freyssinet et al. 2005), although it is also
475 possible that minute Fe-(hydr)oxides physically associated with serpentine have
476 concentrated Ni in our samples. Further microscopic observations or spectroscopic

477 analyses are needed to investigate this possibility.

478 At Tagaung, the occurrence of Mg–Fe–Ni silicates in the saprolite layers (Fig. 7k)
479 resembles the occurrence of Ser-I in the bedrock sample (Fig. 3b), which may indicate
480 that the Mg–Fe–Ni silicates also formed after Ser-I. The SEM–EDS results indicate that
481 the atomic ratio of (Mg + Fe + Ni)/Si in the Mg–Fe–Ni silicates is in the range of 0.9–1.3,
482 which is higher than the ideal chemical composition of smectite (0.5–0.8), and closer to
483 that of serpentine (1.5). Furthermore, because the XRD profiles for the saprolite layer
484 samples from Tagaung indicate the presence of serpentine (Fig. 4c), most Mg–Fe–Ni
485 silicates can be identified as serpentine, namely Ser-II.

486

487 Implications for the formation of high-grade Ni laterite ore deposits in Myanmar

488 This study has shown that Ni fixation to smectite may be one of the most important
489 processes for Ni enrichment in the weathering profile at Tagaung. Because Ni-smectite
490 replaces orthopyroxene, the abundance of pyroxene in bedrock is likely to be one of the
491 most important factors in the formation of high-grade Ni ores in Myanmar. In addition,
492 our results suggest that Ni-rich pore water governs the formation of Ni-smectite during
493 dissolution of pyroxene. Since olivine contains the highest amount of Ni amongst the
494 primary minerals in the bedrock, it should have been the source of Ni, although Ni might
495 have been transferred among different generations of silicate minerals, particularly
496 smectite. We propose, therefore, that high-grade Ni laterite deposits may be developed in
497 Myanmar, or under equivalent climatic conditions, on bedrock composed of both olivine
498 and pyroxene (harzburgite) that is either not serpentinized or partially serpentinized.

499 Although Schellmann (1989b) showed that serpentine was the dominant constituent
500 in a saprolite layer in the Tagaung Taung deposit, our study demonstrates that smectite is

501 the main mineral hosting Ni in the saprolite layer. Tauler et al. (2017) also found Ni-rich
502 smectite at Loma Ortega in the Falcondo mining district, Dominican Republic. They
503 reported an unusual Ni laterite deposit that appears to be a hybrid of the hydrous Mg and
504 clay silicate types of deposits. We propose that the Tagaung Taung deposit is also a hybrid
505 deposit, although dominated by the clay silicate end-member, because smectite is more
506 abundant than at Loma Ortega. However, the crystal chemistry of smectite and its
507 occurrence in the weathering profiles appear to be distinct from typical clay silicate-type
508 deposits (Ca- and Al-bearing nontronite; Gaudin et al. 2004; Mano et al. 2014; Putzolu et
509 al. 2020), which is likely due to the dissolution of plagioclase. Such Ni laterite deposits
510 should be further investigated.
511
512 **Conclusions**
513 We conducted mineralogical and geochemical analyses of two weathering profiles
514 (Budaung and Tagaung) developed on different bedrocks in central Myanmar to
515 understand the processes of formation of high-grade ores in a Ni laterite deposit. Several
516 conclusions are summarized below:
517 • Whole-rock major element analyses indicate that Si was retained relative to Fe and
518 Al in the weathering profiles at Budaung and Tagaung. This is probably due primarily
519 to the climatic conditions of Myanmar. Nickel is highly enriched (up to 4.89 wt.%
520 NiO) in the saprolite layers at Tagaung, whereas the saprolite layers at Budaung only
521 contain up to 1.55 wt.% NiO.
522 • Mass balance calculations suggest that the Ni enrichment at Tagaung has been less
523 constrained by Fe mobilization. This is consistent with the mineralogy of weathering
524 products in the laterite layer, which contains Fe–Al silicates with low Ni contents.

Therefore, Ni enrichment in the saprolite layer at Tagaung might have been governed more by the Ni fixation capacity of weathering products and the timing of their formation.

- The dominant weathering product at Tagaung is smectite. This suggests that in Myanmar deposits, smectite has a higher Ni fixation capability than Ser-II. Saprolite layer at Tagaung is characterized by Fe-smectite (<10 wt.% NiO) and Ni-smectite (>10 wt.% NiO). Detailed SEM observations indicate that Ni-smectite formed only as a replacement product of orthopyroxene, whereas Fe-smectite formed from either olivine or orthopyroxene.
- Smectite at Budaung does not concentrate Ni as much as Ni-smectite at Tagaung. This suggests that the Ni concentration in pore water, governed by dissolution of olivine during the formation of smectite, controlled the Ni contents of smectite.

Therefore, our study implies that, under the climatic conditions of Myanmar, smectite-rich, high-grade Ni ores form in saprolite layers developed on unaltered or partly serpentinized harzburgite bedrocks containing olivine and pyroxene.

Acknowledgments

We thank Tin Tun and Soe Yi for their assistance with fieldwork in the Tagaung Taung mining area. We also thank A. Matsumoto and T. Endo for their technical assistance with the XRF and EPMA analyses. Constructive comments by Editor-in-Chief G. Beaudoin and Associate Editor R. Romer, as well as an anonymous reviewer, greatly improved the manuscript and are appreciated.

Appendix A. Supplementary Information

549 Supplementary data for this article can be found online at
550 https://doi.org/xxxxxxxxxxxxxx.
551
552 **Declarations**
553 Funding: This study was supported by a Joint Research Grant from the "Nanotechnology
554 Platform" Program of the Ministry of Education, Culture, Sports, Science, and
555 Technology (MEXT) of Japan, and the Japan Society for the Promotion of Science (JSPS)
556 KAKENHI Funds (17H03502 and 20H00184).
557
558 Conflicts of interests: The authors have no conflicts of interest to declare that are relevant
559 to the content of this article
560
561 Authors' contributions: All authors contributed to the study conception and design.
562 Material preparation, data collection, and analysis were performed by Akaya Murofushi,
563 Tsubasa Otake, Kenzo Sanematsu, Kyaw Zay Ya, and Akane Ito. The first draft of the
564 manuscript was written by Ayaka Murofushi and Tsubasa Otake, and all authors
565 commented on subsequent versions of the manuscript. All authors read and approved the
566 final manuscript.
567
568 **Figure Captions**
569
570 **Figure 1.** (a) Location of the Western Ophiolite Belt (WOB), Central Ophiolite Belt
571 (COB), and Eastern Ophiolite Belt (EOB) in Myanmar (after Hla Htay et al. 2017). (b)
572 Geological map of the study area (after MGS 2014). (i) and (ii) locate the Budaung and

573 Tagaung weathering profiles in the Kyaukpahto and Tagaung Taung areas, respectively.

574

575 **Figure 2.** Weathering profiles at (a) Budaung and (b) Tagaung.

576

577 **Figure 3.** Photomicrographs of bedrocks. (a) Serpentine (Ser) at Budaung. (b) Partly
578 serpentinized olivine (Ol) at Tagaung. (c) Large unaltered orthopyroxene (OPX) crystal
579 at Tagaung.

580

581 **Figure 4.** X-ray diffractograms of samples from the weathering profiles. (a) Randomly
582 oriented samples and (b) oriented <2 μm fraction of saprolite samples from Budaung. (c)
583 Randomly oriented samples from Tagaung and (d) an enlarged view of part of (c) to show
584 the 060 reflection.

585

586 **Figure 5.** Depth profiles showing the whole-rock geochemical compositions and mass
587 transfer coefficients ($\tau_{j,Ti}$ values) of major elements at (a) Budaung and (b) Tagaung.

588

589 **Figure 6.** Mineral chemistry of weathering products at Budaung and Tagaung. (a) NiO
590 contents and (b) (NiO–Fe_2O_3–MgO) molar ternary plot of serpentine II (Ser-II) and
591 smectite from the lower and upper saprolite layers of Budaung. (c) Relationship between
592 NiO and Fe_2O_3 contents in Ni-smectite at Tagaung. (d) Relationship between NiO and
593 Fe_2O_3 contents in Fe-smectite (i.e., low-Ni smectite) derived from olivine (coexisting
594 with Mg–Fe–Ni silicates) and pyroxene (coexisting with Ni-smectite) at Tagaung. Shaded
595 area in (d) shows the chemical composition of Mg–Fe–Ni silicates (M–F–N-S) estimated
596 by SEM–EDS.

Figure 7. Backscatter electron (BSE) images of weathering products. (a) Ser-I and Ser-II and (b) Fe-Mg Sme surrounded by Ser-II in the lower saprolite, (c) Ser-II forming vein-like structure and (d) Fe-Mg Sme surrounded by Ser-II in the upper saprolite, and (e) Qz and Fe-Al silicates in the laterite layers at Budaung. (f, g) Ni-Sme and Fe-Sme occurring near the remnants of Opx and (h) Fe-Sme and Ol surrounded by M-F-N-S in the lower saprolite, and (i, j) Ni-Sme together with porous Fe-Sme and (k) particulate Fe-Sme surrounded by M-F-N-S in the upper saprolite, and (l) Qz and Fe-Al silicates in the laterite layers at Tagaung. Ser-I = serpentine-I; Ser-II = serpentine-II; Fe–Mg Sme = Fe–Mg smectite; Qz = quartz; Opx = orthopyroxene; Ni-Sme = Ni-smectite; Fe-Sme = Fe-smectite; Ol = olivine; M–F–N–S = Mg–Fe–Ni silicates.

Figure 8. (a) Molar Si–(Fe + Al)–Mg ternary diagram for the bulk chemical composition of ultramafic rocks along the weathering profiles and (b) the amounts of Fe and Ni gained in the saprolite layers at Budaung and Tagaung as compared with those in Indonesia (Ito et al. 2021). Dashed arrow in (a) is a general weathering trend for ultramafic rocks in Indonesia and other regions (Aiglsperger et al. 2016; Ito et al. 2021).

Figure 9. Mg–Ni–Fe ternary diagrams showing the occupancy of cations in the octahedral sheets of smectites derived from (a) olivine and (b) pyroxene at Tagaung. Triangles are primary mineral data (i.e., olivine and orthopyroxene). Aluminum is not included in the diagram because it was negligible in content compared with the other three components.

References

621 Aiglsperger T, Proenza JA, Lewis JF, Labrador M, Svojtka M, Rojas-Purón A, Longo F,
622 Ďurišová J (2016) Critical metals (REE, Sc, PGE) in Ni laterites from Cuba and
623 the Dominican Republic. Ore Geol Rev 73:127-147.
624 https://doi.org/10.1016/j.oregeorev.2015.10.010.

625 Brimhall GH, Dietrich WE (1987) Constitutive mass balance relations between
626 chemical composition, volume, density, porosity, and strain in metasomatic
627 hydrochemical systems: Results on weathering and pedogenesis. Geochim
628 Cosmochim Acta 51:567-587. https://doi.org/10.1016/0016-7037(87)90070-6.

629 Butt CRM, Cluzel D (2013) Nickel laterite ore deposits: Weathered serpentinites.
630 Elements 9:123-128. https://doi.org/10.2113/gselements.9.2.123.

631 Chikanda F, Otake T, Ohtomo Y, Ito A, Yokoyama TD, Sato T (2019) Magmatic-
632 hydrothermal processes associated with Rare Earth Element enrichment in the
633 Kangankunde Carbonatite Complex, Malawi. Minerals 9:442.
634 https://doi.org/10.3390/min9070442.

635 Colin F, Nahon D, Trescases.J.J, Melefi AJ (1990) Lateritic weathering of pyroxenites at
636 Niquelandia, Goias, Brazil: The supergene behavior of nickel. Econ Geol
637 85:1010-1023. https://doi.org/10.2113/gsecongeo.85.5.1010.

638 Decarreau A, Colin F, Herbillon A, Manaceau A, Nahon D, Paquet H, Trauth-Badaud D,
639 Trescases JJ (1987) Domain segregation in Ni-Fe-Mg smectites. Clays Clay
640 Miner 35:1-10. https://doi.org/10.1346/CCMN.1987.0350101.

641 Deer WA, Howie RA, Zussman J (1982) Rock-forming Minerals: Orthosilicates.
642 Geological Society of London.

643 Deer WA, Howie RA, Zussman J (2009) Rock-forming Minerals: Layered Silicates
644 Excluding Micas and Clay Minerals. Geological Society of London.

645 Delina RE, Arcilla C, Otake T, Garcia JJ, Tan M, Ito A (2020) Chromium occurrence in
646 a nickel laterite profile and its implications to surrounding surface waters. Chem
647 Geol 558:119863. https://doi.org/10.1016/j.chemgeo.2020.119863.

648 Dublet G, Juillot F, Morin G, Fritsch E, Fandeur D, Ona-Nguema G, Brown GE (2012)
649 Ni speciation in a New Caledonian lateritic regolith: A quantitative X-ray
650 absorption spectroscopy investigation. Geochim Cosmochim Acta 95:119-133.
651 https://doi.org/10.1016/j.gca.2012.07.030.

652 Eggleton RA (1975) Nontronite topotaxial after hedenbergite. Am Mineral 60:1063-
653 1068.

654 Elias M (2002) Nickel laterite deposits – geological overview , resources and
655 exploitation In: Cooke D, Pongratz J (eds) Giant Ore Depositis: Characteristics,
656 genesis and exploration. University of Tasmania, Hobart, pp 205-220.

657 Fan R, Gerson AR (2015) Synchrotron micro-spectroscopic examination of Indonesian
658 nickel laterites. Am Mineral 100:926-934. https://doi.org/10.2138/am-2015-

5093.

Freyssinet P, Butt CRM, Morris RC (2005) Ore-forming processes related to lateritic weathering In: Hedenquist JW, Thompson JFH, Goldfarb RJ, Richards JP (eds) Economic Geology: One Hundredth Anniversary Volume. Society of Economic Geologists, Littleton, CO, pp 681-722.

Gaudin A, Grauby O, Noack Y, Decarreau A, Petit S (2004) Accurate crystal chemistry of ferric smectites from the lateritic nickel ore of Murrin Murrin (Western Australia). I. XRD and multi-scale chemical approaches. Clay Miner 39:301-315. http://dx.doi.org/10.1180/0009855043930136.

Gaudin A, Decarreau A, Noack Y, Grauby O (2005) Clay mineralogy of the nickel laterite ore developed from serpentinised peridotites at Murrin Murrin, Western Australia. Aust J Earth Sci 52:231-241. https://doi.org/10.1080/08120090500139406.

Gleeson SA, Butt CRM, Elias M (2003) Nickel laterites: A review. SEG Newslett 54:9-16.

Goldich SS (1984) Determination of ferrous iron in silicate rocks. Chem Geol 42:343-347. https://doi.org/10.1016/0009-2541(84)90027-5.

Golightly JP (1981) Nickeliferous Laterite Deposits In: Skinner BJ (ed) Economic Geology: Seventy-Fifth Anniversary Volume. Economic Geology Publishing Company, El Paso, TX, pp 710-735.

Golightly JP (2010) Progress in understanding the evolution of nickel laterites In: Goldfarb RJ, Marsh, E. E. and Monecke, T. (ed) The Challenge of Finding New Mineral Resources: Global Metallogeny, Innovative Exploration, and New Discoveries. Society of Economic Geologists, Denver, CO, pp 451-485.

Hla Htay, Khin Zaw, Than Than Oo (2017) The mafic-ultramafic (ophiolitic) rocks of Myanmar In: Barber AJ, Khin Zaw, Crow MJ (eds) Myanmar: Geology, Resources and Tectonics. The Geological Society London, Bath, UK, pp 117-141.

Ito A, Otake T, Maulana A, Sanematsu K, Sufriadin, Sato T (2021) Geochemical constraints on the mobilization of Ni and critical metals in laterite deposits, Sulawesi, Indonesia: A mass-balance approach. Resour Geol 71:255-282. https://doi.org/10.1111/rge.12266.

Khin Zaw, Win Swe, Barber AJ, Crow MJ, Yin Yin Nwe (2017) Introduction to the geology of Myanmar In: Barber AJ, Khin Zaw, Crow MJ (eds) Myanmar: Geology, Resources and Tectonics. The Geological Society London, Bath, UK, pp 1-17.

Kyser TK, O'Hanley DS, Wicks FJ (1999) The origin of fluids associated with serpentinization processes: Evidence from stable-isotope compositions. Can

698 Mineral 37:223-237.

699 Mano ES, Caner L, Petit S, Chaves AP, Mexias AS (2014) Mineralogical
700 characterization of Ni-bearing smectites from Niquelândia, Brazil. Clays Clay
701 Miner 62:324-335. https://doi.org/10.1346/CCMN.2014.0620406.

702 Maurizot P, Sevin B, Iseppi M, Giband T (2019) Nickel-bearing laterite deposits in
703 accretionary context and the case of New Caledonia: From the large-scale
704 structure of earth to our everyday appliances. GSA Today 29.
705 https://doi.org/10.1130/GSATG364A.1.

706 Meunier A (2005) Clays. Springer-Verlag, Berlin Heidelberg.

707 MGS (2014) Geological map of Myanmar. Myanmar Geosciences Society, Yangon.

708 Morimoto N (1988) Nomenclature of pyroxenes. Mineral Petrol 39:55-76.

709 Pereira MD, Peinado M, Blanco JA, Yenes M (2008) Geochemical characterization of
710 serpentinites at Cabo Ortegal, Northwestern Spain. Can Mineral 46:317-327.
711 https://doi.org/10.3749/canmin.46.2.317.

712 Putzolu F, Abad I, Balassone G, Boni M, Mondillo N (2020) Ni-bearing smectites in the
713 Wingellina laterite deposit (Western Australia) at nanoscale: TEM-HRTEM
714 evidences of the formation mechanisms. Applied Clay Science 196:105753.
715 https://doi.org/10.1016/j.clay.2020.105753.

716 Roqué-Rosell J, Villanova-de-Benavent C, Proenza JA (2017) The accumulation of Ni
717 in serpentines and garnierites from the Falcondo Ni-laterite deposit (Dominican
718 Republic) elucidated by means of μXAS. Geochim Cosmochim Acta 198:48-69.
719 https://doi.org/10.1016/j.gca.2016.11.004.

720 Schellmann W (1989a) Allochthonous surface alteration of Ni-laterites. Chem Geol
721 74:351-364. https://doi.org/10.1016/0009-2541(89)90044-2.

722 Schellmann W (1989b) Composition and origin of lateritic nickel ore at Tagaung Taung,
723 Burma. Miner Deposita 168:161-168. https://doi.org/10.1007/BF00206438.

724 Shimbashi M, Sato T, Yamakawa M, Fujii N, Otake T (2018) Formation of Fe- and Mg-
725 rich smectite under hyperalkaline conditions at Narra in Palawan, the
726 Philippines. Minerals 8. https://doi.org/10.3390/min8040155.

727 Soe Win, Than Htay, Tin Lin, Win Myint Law (2014) A Case Study of Tagaung Taung
728 Nickel Laterite Deposit: From Prospect to a Mine. Unpublished Report, Yangon,
729 32 pp

730 Tauler E, Lewis JF, Villanova-de-Benavent C, Aiglsperger T, Proenza JA, Domènech C,
731 Gallardo T, Longo F, Galí S (2017) Discovery of Ni-smectite-rich saprolite at
732 Loma Ortega, Falcondo mining district (Dominican Republic): geochemistry
733 and mineralogy of an unusual case of “hybrid hydrous Mg silicate – clay
734 silicate” type Ni-laterite. Miner Deposita 52:1011-1030.

https://doi.org/10.1007/s00126-017-0750-8.

Thorne RL, Roberts S, Herrington R (2012) Climate change and the formation of nickel laterite deposits. Geology 40:331-334. https://doi.org/10.1130/G32549.1.

Tupaz CAJ, Watanabe Y, Sanematsu K, Echigo T (2020) Mineralogy and geochemistry of the Berong Ni-Co laterite deposit, Palawan, Philippines. Ore Geol Rev 125:103686. https://doi.org/10.1016/j.oregeorev.2020.103686.

Villanova-de-Benavent C, Domènech C, Tauler E, Galí S, Tassara S, Proenza JA (2017) Fe–Ni-bearing serpentines from the saprolite horizon of Caribbean Ni-laterite deposits: new insights from thermodynamic calculations. Miner Deposita 52:979-992. https://doi.org/10.1007/s00126-016-0683-7.

Wilson MJ, Deer WA, Howie RA, Zussman J (2013) Rock-forming Minerals: Sheet Silicates: Clay Minerals. Geological Society of London.

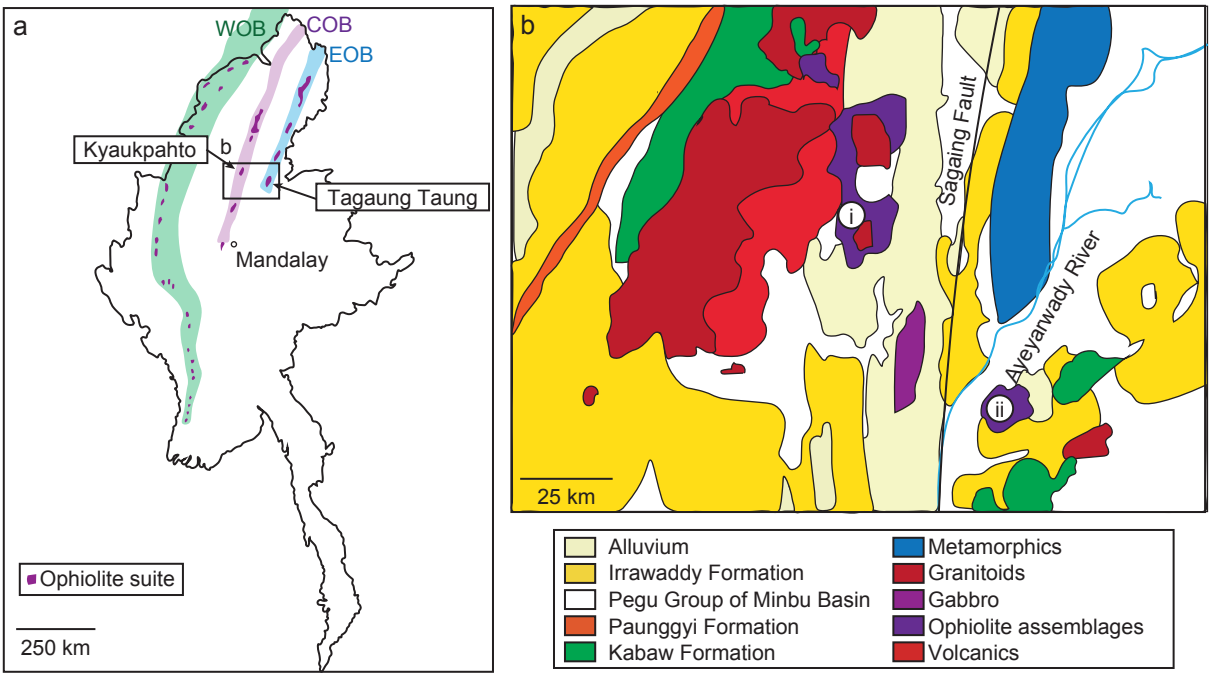
a
WOB
COB
EOB
Kyaukpahto
b
Tagaung Taung
Mandalay
Ophiolite suite
250 km
b
Sagaing Fault
Ayeyarwady River
i
ii
25 km
Alluvium
Irrawaddy Formation
Pegu Group of Minbu Basin
Paunggyi Formation
Kabaw Formation
Metamorphics
Granitoids
Gabbro
Ophiolite assemblages
Volcanics

Fig. 1

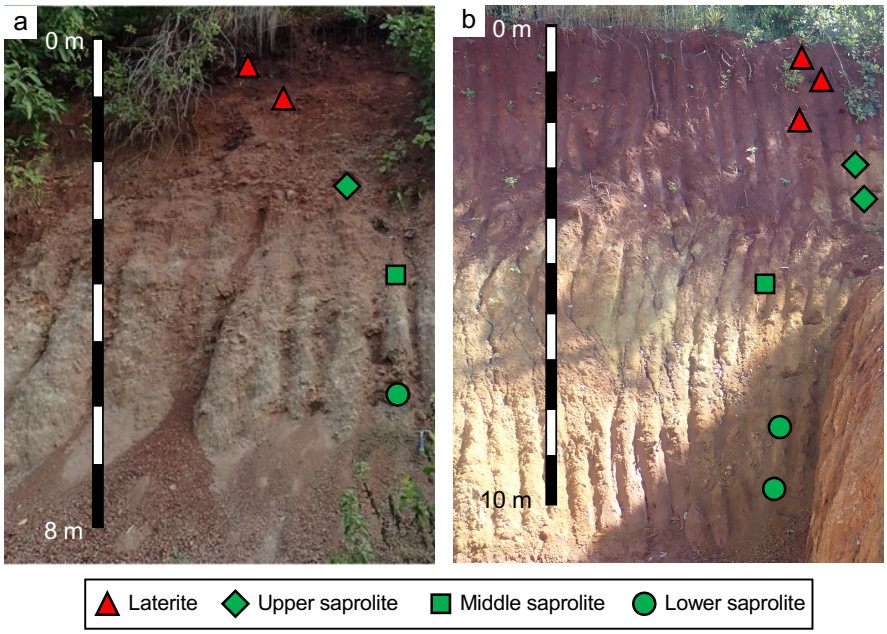
a
0 m
8 m
b
0 m
10 m
Laterite
Upper saprolite
Middle saprolite
Lower saprolite

Fig. 2

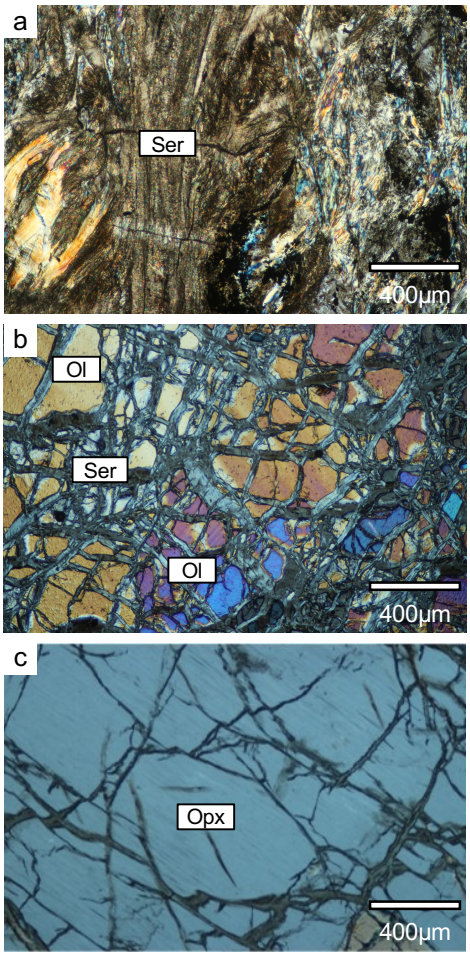

Fig. 3

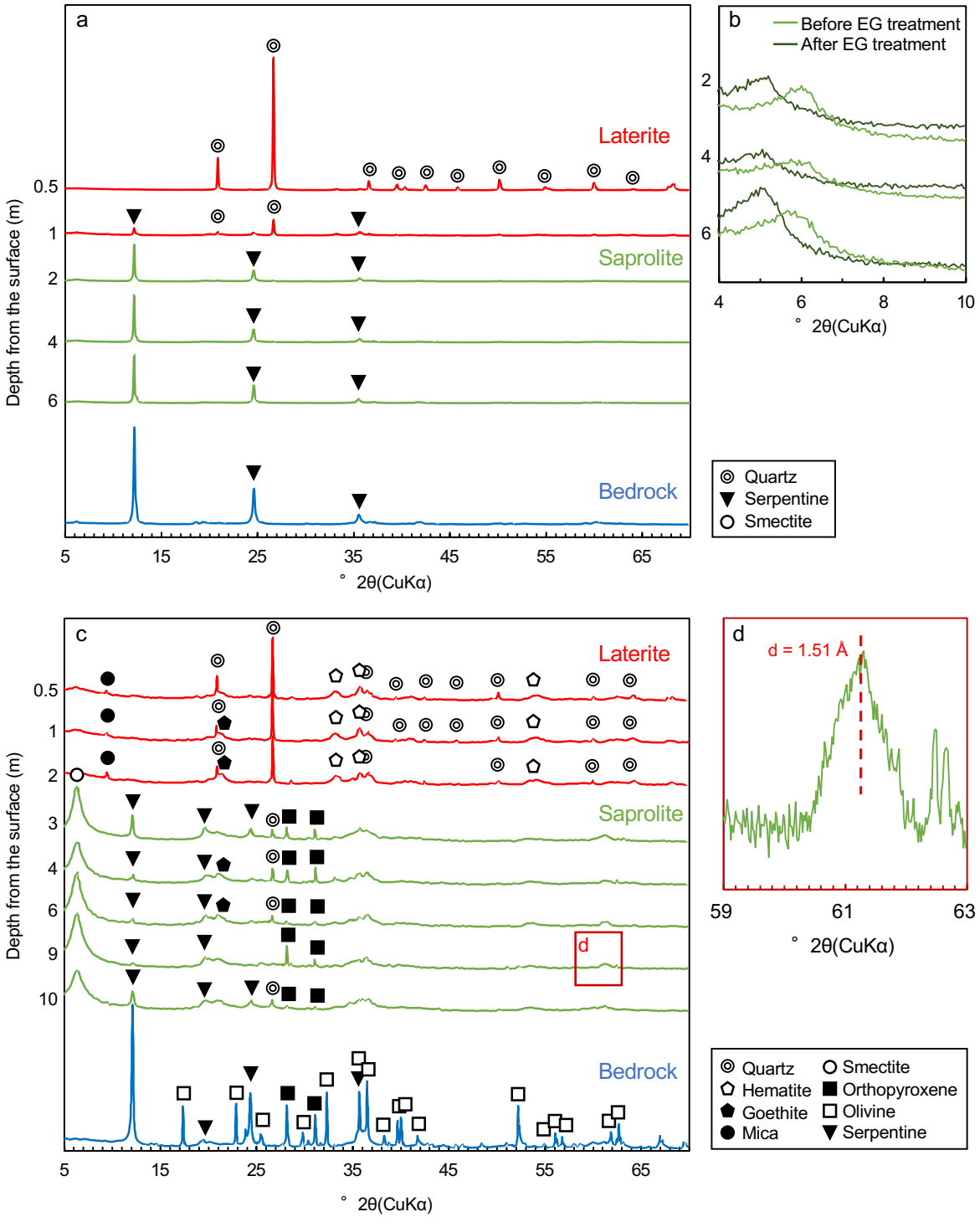
a
Laterite
Saprolite
Bedrock
Depth from the surface (m)
0.5
1
2
4
6
5
15
25
35
45
55
65
° 2θ(CuKα)
Quartz
Serpentine
Smectite
b
Before EG treatment
After EG treatment
2
4
6
4
6
8
10
° 2θ(CuKα)
c
Laterite
Saprolite
Bedrock
Depth from the surface (m)
0.5
1
2
3
4
6
9
10
d
5
15
25
35
45
55
65
° 2θ(CuKα)
Quartz
Hematite
Goethite
Mica
Smectite
Orthopyroxene
Olivine
Serpentine
d
d = 1.51 Å
59
61
63
° 2θ(CuKα)

Fig. 4

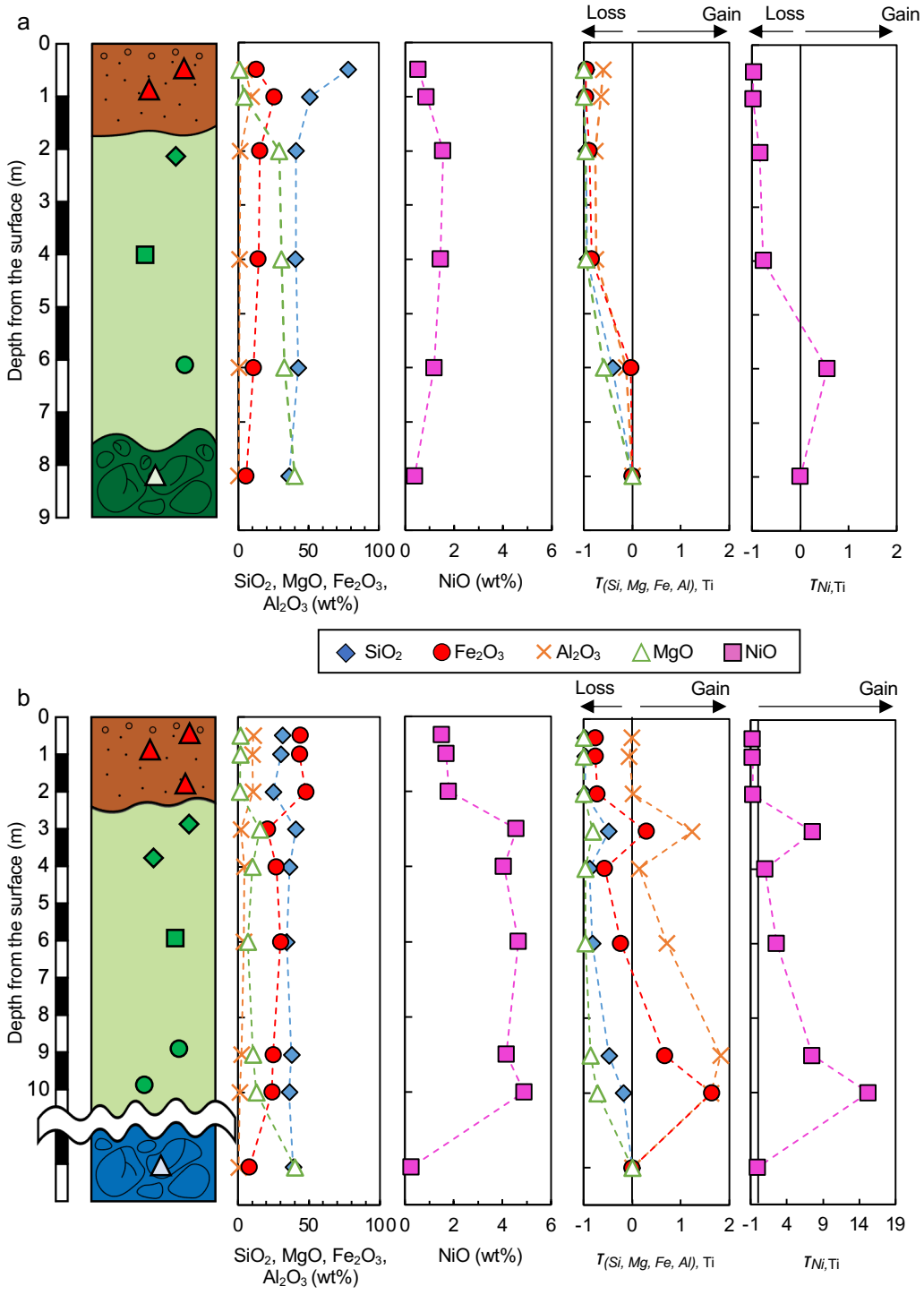
a
b
Depth from the surface (m)
Loss
Gain
SiO2
Fe2O3
Al2O3
MgO
NiO
SiO2, MgO, Fe2O3, Al2O3 (wt%)
NiO (wt%)
T(Si, Mg, Fe, Al), Ti
TNi,Ti

Fig. 5

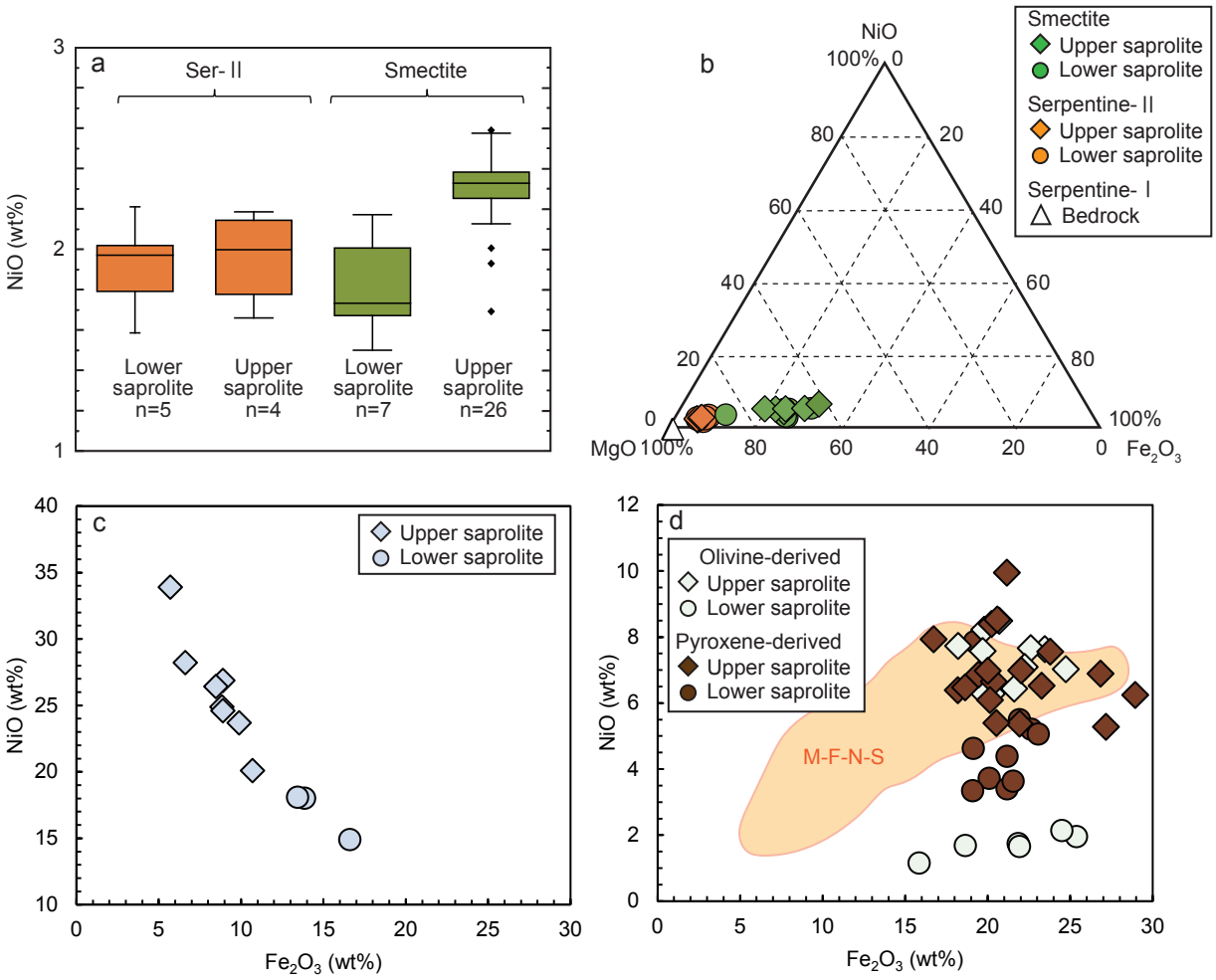
a
Ser- II
Smectite
NiO (wt%)
Lower saprolite n=5
Upper saprolite n=4
Lower saprolite n=7
Upper saprolite n=26
b
NiO
MgO
Fe2O3
Smectite
Upper saprolite
Lower saprolite
Serpentine- II
Upper saprolite
Lower saprolite
Serpentine- I
Bedrock
c
Upper saprolite
Lower saprolite
NiO (wt%)
Fe2O3 (wt%)
d
Olivine-derived
Upper saprolite
Lower saprolite
Pyroxene-derived
Upper saprolite
Lower saprolite
M-F-N-S
NiO (wt%)
Fe2O3 (wt%)

Fig. 6

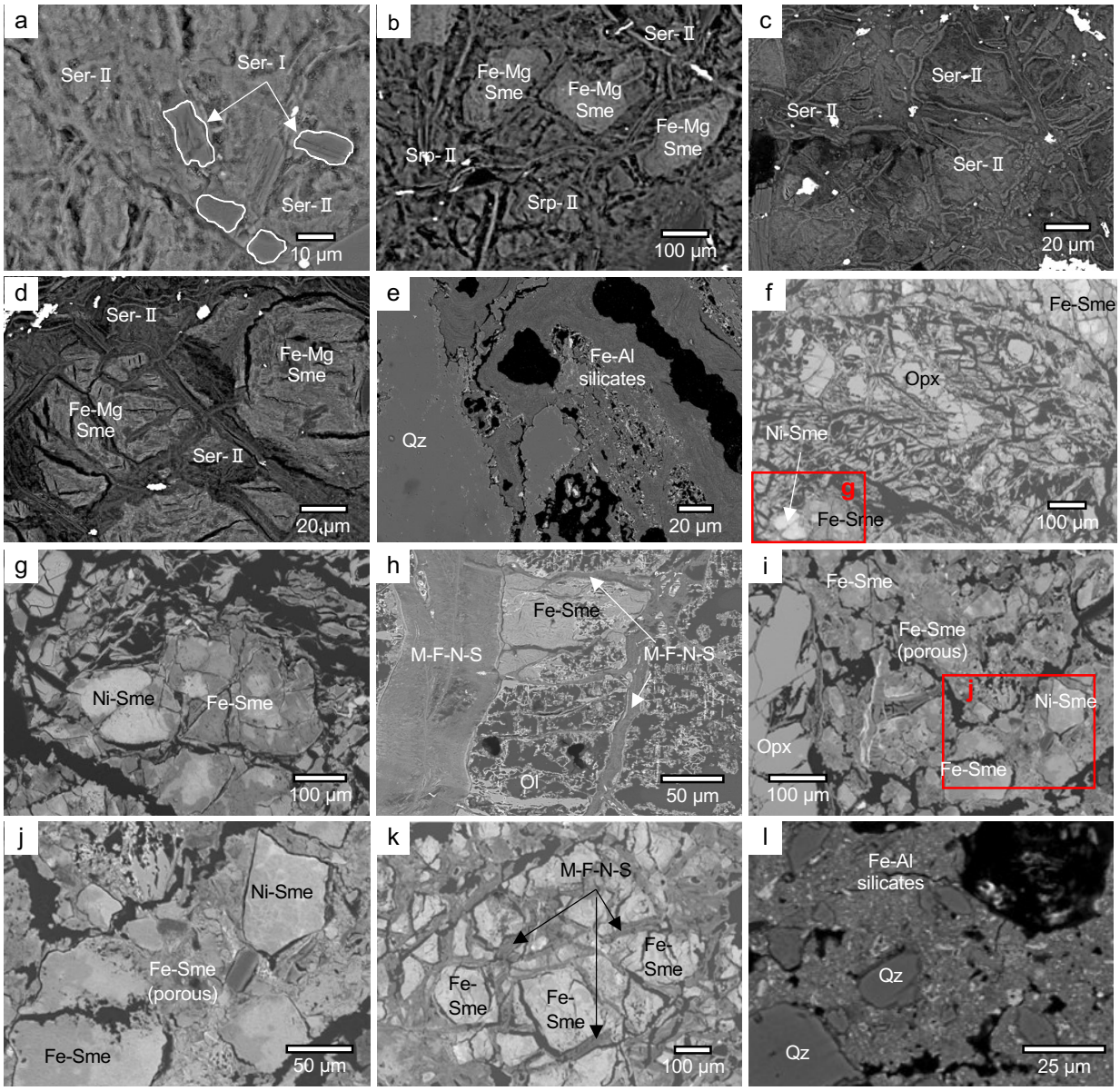
a
Ser-Ⅱ
Ser-Ⅰ
Ser-Ⅱ
10 μm
b
Ser-Ⅱ
Fe-Mg Sme
Fe-Mg Sme
Fe-Mg Sme
Srp-Ⅱ
Srp-Ⅱ
100 μm
c
Ser-Ⅱ
Ser-Ⅱ
Ser-Ⅱ
20 μm
d
Ser-Ⅱ
Fe-Mg Sme
Fe-Mg Sme
Ser-Ⅱ
20 μm
e
Fe-Al silicates
Qz
20 μm
f
Fe-Sme
Opx
Ni-Sme
g
Fe-Sme
100 μm
g
Ni-Sme
Fe-Sme
100 μm
h
Fe-Sme
M-F-N-S
M-F-N-S
Ol
50 μm
i
Fe-Sme
Fe-Sme (porous)
j
Ni-Sme
Opx
Fe-Sme
100 μm
j
Ni-Sme
Fe-Sme (porous)
Fe-Sme
50 μm
k
M-F-N-S
Fe-Sme
Fe-Sme
Fe-Sme
100 μm
l
Fe-Al silicates
Qz
Qz
25 μm

Fig. 7

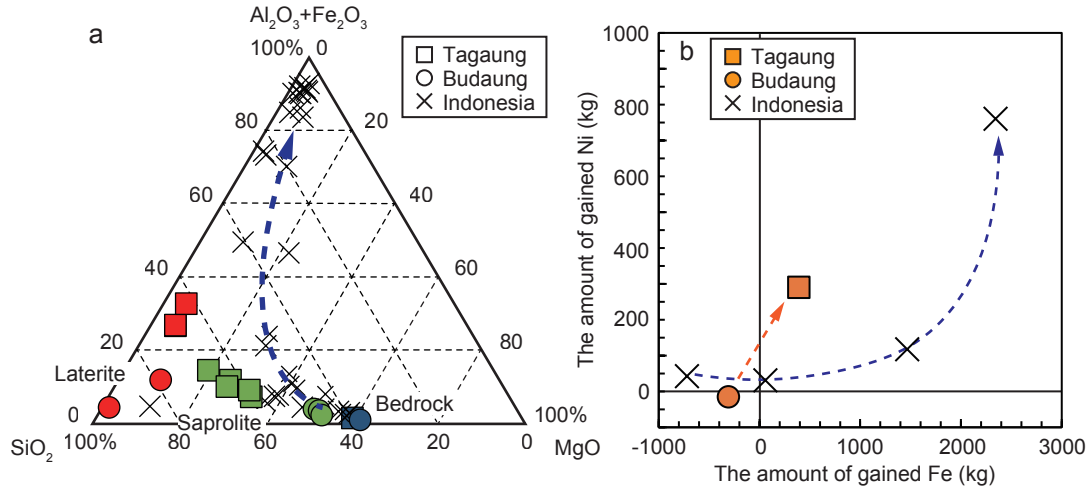
a
$Al_2O_3+Fe_2O_3$
100%
0
80
20
60
40
40
60
20
80
0
100%
SiO_2
100%
80
60
40
20
0
MgO
Tagaung
Budaung
Indonesia
Laterite
Saprolite
Bedrock
b
Tagaung
Budaung
Indonesia
The amount of gained Ni (kg)
1000
800
600
400
200
0
-1000
0
1000
2000
3000
The amount of gained Fe (kg)

Fig. 8

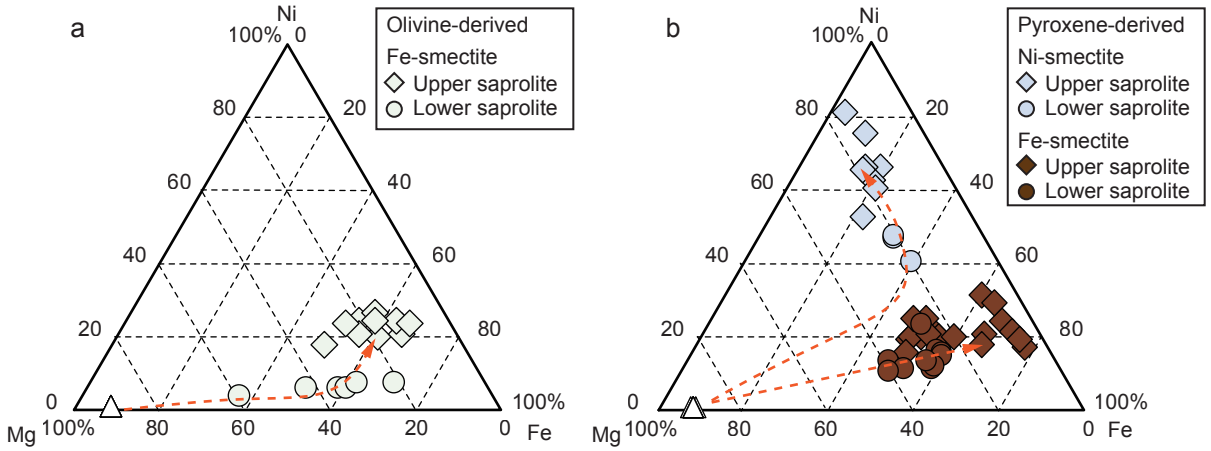
a
Ni
100% 0
80
20
60
40
40
60
20
80
0
100%
Mg 100% 80 60 40 20 0 Fe
Olivine-derived
Fe-smectite
Upper saprolite
Lower saprolite
b
Ni
100% 0
80
20
60
40
40
60
20
80
0
100%
Mg 100% 80 60 40 20 0 Fe
Pyroxene-derived
Ni-smectite
Upper saprolite
Lower saprolite
Fe-smectite
Upper saprolite
Lower saprolite

Fig. 9